Photoacoustics 38 (2024) 100631

Contents lists available at ScienceDirect

Photoacoustics

journal homepage: www.elsevier.com/locate/pacs

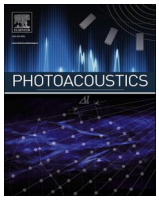

Probe fusion all-optic OCT-PAM dual-mode imaging system for biomedical imaging

Ning Ding [a], Huiwen Jiang [a], Ben Xiang [a], Yao Yu [b,c], Cheng Ji [d], Jian Liu [b,c], Yuqian Zhao [b,c], Jingmin Luan [e], Yanqiu Yang [b,c], Yi Wang [b,c], Zhenhe Ma [b,c,*]

[a] College of Information Science and Engineering, Northeastern University, Shenyang 110819, China
[b] School of Control Engineering, Northeastern University at Qinhuangdao, Qinhuangdao 066004, china
[c] Hebei Key Laboratory of Micro-Nano Precision Optical Sensing and Measurement Technology, Qinhuangdao 066004, China
[d] Qinhuangdao Haigang Hospital, Qinhuangdao 066004, China
[e] School of Computer and Communication Engineering, Northeastern University at Qinhuangdao, Qinhuangdao 066004, China

ARTICLE INFO

Keywords:
Photoacoustic imaging
Optical coherence tomography
Dual mode imaging
Optical coherence tomography angiography

ABSTRACT

We proposed a non-contact photoacoustic (PA) detection method using spectral domain optical coherence tomography (SDOCT). Two interference spectrums (A-lines) were acquired before and after the PA excitation with SDOCT. PA signal propagated within the sample causing the vibration. The vibration inner the sample introduced phase change between the acquired two A-lines. Thus, the PA signal can be detected by evaluating the difference in phase between the two A-lines. Based on the method, an OCT-PAM dual-mode imaging system was constructed. In the system, SDOCT served as the detection unit for PAM. Thus, the combination of the two imaging modalities was simplified. Another advantage of the system is that it realizes non-contact all-optic detection, which is attractive for biomedical imaging. Using the system, we imaged phantoms of carbon fibers, asparagus leaves and human hairs. Furthermore, the cortical vasculature of rat was imaged *in vivo* and the flow status was evaluated quantitatively.

1. Introduction

Over the past few years, optical imaging techniques have developed fast and become increasingly important in biological research and medical diagnostics. Optical coherence tomography (OCT) is a well-established technique in the biomedical field, that relies on low-coherence interference for optical imaging. It has depth-resolved ability and can provide μm-scale optical scattering contrast [1–3]. OCT technology has gradually developed from the initial intensity-based structural imaging to functional imaging, including the Doppler OCT (DOCT) [4], polarization-sensitive OCT (PS-OCT) [5], and OCT angiography (OCTA) [6], etc. Due to the advantages of combining optical contrast and ultrasound resolution, photoacoustic imaging (PAI) is attracting increasing interest [7–11]. It detects the optical absorption of samples depending on the photoacoustic (PA) effect, a physical mechanism by which absorbed optical power is converted into the acoustic wave [12]. As one type of implementation of PAI, photoacoustic microscopy (PAM) has the advantage of providing micron-scale spatial resolution and rich optical-absorption contrast [13–15].

Any single type of imaging technology has its limitations and is not able to reflect the full range of physiological and pathological information [16]. For the past several decades, the emergence of multimodal optical imaging technology has enabled the acquisition of more comprehensive information about the structure and functions of biological tissues, facilitating biomedical research and clinical diagnosis [17]. Scattering and absorption are two major optical characteristics of biological tissue, corresponding to OCT and PAM, respectively. An imaging system that combines OCT and PAM can provide complementary contrasts for imaging [18,19]. However, acoustic coupling between the sample and transducer is a fundamental requirement in traditional PA imaging, which limits the potential applications (such as brain surgeries [20] and burn diagnostics [21]). On the other hand, the transducer used in PAM obstructs OCT scanning [22]. Therefore, finding an effective non-contact photoacoustic detection method to replace the traditional ultrasonic transducer is one of the focuses of current research.

One solution for non-contact PAM is to detect the PA signal using optical interference techniques. In some non-contact photoacoustic imaging studies, Mach-Zehnder interferometers and Fabry-Perot

* Corresponding author at: School of Control Engineering, Northeastern University at Qinhuangdao, Qinhuangdao 066004, china.
E-mail address: mazhenhe@163.com (Z. Ma).

https://doi.org/10.1016/j.pacs.2024.100631
Received 25 April 2024; Received in revised form 29 May 2024; Accepted 28 June 2024
Available online 1 July 2024

interferometers were employed as substitutes for traditional ultrasonic transducers [23–27]. It should be noted that these techniques also present difficulties when combined with OCT systems, because of the bulky configuration of the optics, the loss of sensitivity, or the disturbance of the dispersion [28]. J. Eom et al. proposed an all-fiber-based dual-modal imaging system that combined non-contact photoacoustic imaging and OCT. The PA signals were remotely measured by utilising a fibre interferometer as an ultrasound detector. The all-fibre-optic system has promising potential in minimally invasive and endoscopic imaging [29]. Yi Wang et al. applied a homodyne interferometric method based on the Michelson interferometer for PA signal detection and realized vascular imaging using mouse auricle as a sample [30,31]. The optical path design of this method is simple and easy to combine with other imaging modes. Based on this technology, Zhongjiang Chen et al. realized multi-modal imaging of the OCT-PAM-fluorescence imaging [28]. To maximize the sensitivity of the system, it is necessary to acquire the signal near the zero point (the phase is an integer multiple of π). This procedure takes a lot of time, which slows down the imaging speed of the multimodal system. Blatter et al. proposed a methodology for extracting the PA signal from the evolution of the phases over time of the swept source OCT [32]. To reduce the phase noise, multiple acquisitions (each lateral position 200 M-Scans) are required, which limits the imaging speed. Benyamin et al. proposed a method to detect PA signals based on the laser speckle contrast [33]. However, PA signals need to be coupled to the surface of the glass cuvette for detection, which may cause inconvenience to the experiment. In our previous study, we proposed a non-contact PA detection method based on contrast reduction of spectral interference [34]. The method gave the potential to construct an OCT-PAM dual-mode system with a simplified optical design, namely, the detection unit of PAM was replaced by SDOCT. However, the method proposed previously only utilises the interference induced from the surface reflection of the sample for PA detection thus the surface reflection is crucial. The sample must cover a thin layer of water (or oil) film to improve the surface reflection. Water film covering is inconvenient, especially for *in vivo* experiments.

In this paper, we proposed a non-contact PA detection method using SDOCT. Instead of only using single-layer reflection from the surface, the phase variance between two SDOCT A-lines (before and after PA excitation) was used to extract the PA signal. An all-optic non-contact OCT-PAM system was developed based on the proposed method. We imaged phantoms of carbon fibers, asparagus leaves and human hairs using the system. Furthermore, the cortical vasculature of the rat was imaged *in vivo*, and the flow status was evaluated quantitatively. The result demonstrated that the proposed OCT-PAM system can be a useful tool for biomedical imaging.

2. Material and methods

2.1. OCT angiography

In SDOCT, the interference spectrum was acquired by a high-speed line-scan camera. For the sake of simplicity, all non-contributory components were disregarded in the extraction of useful information. The expression for the interference signal is as follows:

$$I(k) = 2S(k)E_R \int_{-\infty}^{\infty} a(z)\cos(2knz + \varphi_0)dz \tag{1}$$

where $S(k)$ denotes the light source spectral density; k represents the wave number; E_R is the reference light amplitude; $a(z)$ is defined as the backscattered light intensity of the sample; z is the sample depth; and φ_0 is the initial phase. Fast Fourier transformation (FFT) was performed on the spectrums to extract backscattering signal distribution. The FFT result of the real sequence is complex, containing amplitude and phase information, which can be formulated as:

$$\widetilde{I}(z) = \widehat{\widehat{I}}(z)\exp(i\varphi(z)) \tag{2}$$

where the amplitude $\widehat{\widehat{I}}(z)$ was used to build structural images, while phase $\varphi(z)$ can be employed to calculate the phase change resulting from the motion.

Based on the amplitude information, OCT angiography (OCTA) can extract the dynamic information of blood flow BF (x, z) by difference operation on images acquired at the same location:

$$BF(x,z) = \widehat{\widehat{I}}(x,z)_{t+\Delta t_B} - \widehat{\widehat{I}}(x,z)_t \tag{3}$$

where, $\widehat{\widehat{I}}(x,z)$ represents the amplitude distribution of OCT B-scan image; Δt_B indicates the interval between the two B scans. Then *en-face* blood vessel distribution map (OCTA image) can be achieved by rending multiple BF (x, z) at different positions. The detailed OCTA description has been described in the previous publication [35].

The calculation of the difference in phase ($\Delta\varphi$) between two A-scans allows for the evaluation of the sample motion [36]. The relationship is as follows:

$$\Delta\varphi = \frac{4\pi n\tau V\cos\theta}{\lambda} \tag{4}$$

where n (~1.3) is the tissue refractive index; the time interval between two adjacent A-scans is defined as τ; θ denotes the Doppler angle; V represents the absolute velocity; λ is the light source centre wavelength. From Eq. (4), it follows that the phase difference ($\Delta\varphi$) is proportional to the motion velocity and can be used for PA signal detection.

2.2. PA signal detection using SDOCT

When a short pulse laser is irradiated on the sample, the absorption of the laser by localized absorbers within the sample generates PA waves through thermoelastic expansion. The following general PA equation describes the generation and propagation of PA waves in the medium [37]:

$$\left(\nabla^2 - \frac{1}{v_s}\frac{\partial^2}{\partial t^2}\right)p(\vec{r},t) = -\frac{\beta}{C_p}\frac{\partial H(\vec{r},t)}{\partial t} \tag{5}$$

where v_s is the sound speed, which is approximately 1480 m/s in water; $p(\vec{r},t)$ represents the rise of acoustic pressure rise at position r and time t; the coefficient of thermal expansion of the volume is symbolised by β; C_p represents the specific heat capacity of the material at constant pressure; and $H(\vec{r},t)$ stands for the heat function. On the left-hand side of Eq. (5), we find the description of the wave propagation in the medium, while the right-hand side represents the source.

PA wave generation and propagation usually require the satisfaction of two basic equations, namely, the equation of thermal expansion [38]:

$$\nabla\cdot\vec{\xi}(\vec{r},t) = -kp(\vec{r},t) + \beta T(\vec{r},t) \tag{6}$$

and the motion equation:

$$\rho\frac{\partial^2}{\partial t^2}\vec{\xi}(\vec{r},t) = -\nabla p(\vec{r},t) \tag{7}$$

where $\vec{\xi}$ represents medium displacement. According to the equation of motion, the pressure generated by a pulsed laser will cause tissue displacement. Traditional PA imaging focused on pressure detection, here we detected the phase variance in SDOCT caused by the propagation of the acoustic wave in the tissue. During the acoustic wave propagation, the interference spectrum of SDOCT can be formulated as:

$$I_{PA}(k) = 2S(k)E_R \int_{-\infty}^{\infty} a(z)\cos(2kn(z+\xi(t)) + \varphi_0)dz \tag{8}$$

Considering that the vibration amplitude of acoustic wave remains much smaller than z and the center wavelength of SDOCT [39], Eq. (8) can be rewritten as:

$$I_{PA}(k) = 2S(k)E_R \int_{-\infty}^{\infty} a(z)\cos\left(2knz + \underbrace{(2kn\xi(t) + \varphi_0)}_{phase\ term}\right)dz \tag{9}$$

According to Eq. (9), $\vec{\xi}$ influences the phase term mainly. After PA excitation, it generates broadband acoustic waves spanning from dozens of kHz to hundreds of MHz [40]. The propagation of multiple frequency components in the sample results in the random variance of the interference phase in SDOCT. The phase variance can be calculated using two SDOCT A-lines (before and after PA excitation).

Using a tungsten wire phantom, we evaluated the phase variance of the OCT signal after the PA excitation (Fig. 1). Tungsten wire was embedded in the agar mixture of intralipid (Fig. 1(a)). The cross-sectional structural image of the OCT B-scan is displayed in Fig. 1(b). Focused on the tungsten wire (yellow dashed line in (b)), the original interference spectrums were acquired and the phase difference was calculated with and without PA excitation (Fig. 1(c)). The blue curve in (c) exhibits the difference in phase between two A-lines without excitation. We can see that the fluctuation of the curve is small, indicating a small phase change at different depths. The red curve in (c) represents the phase difference between two A-lines before and after excitation. Compared with the blue curve, the fluctuation of the red curve is large, indicating that the propagation of acoustic waves causes large phase changes at different depths. Focused on the agar area (dashed pink line in (b)), we also acquired interference spectrums and calculated the phase difference with and without the excitation (Fig. 1(d)). We can see that there is no significant difference between the two curves. Though excitation was performed, the absorption of agar is little and the PA effect is negligible. Thus, the phase between OCT A-lines is also stable with the excitation. Here, we use the standard deviation (STD) of the phase difference for imaging:

$$phase_{std} = \sqrt{\frac{1}{N}\sum_{i=1}^{N}\left(phase_i - \overline{phase}\right)^2} \tag{10}$$

where i is the index of N; N is the number of pixels used for the STD calculation; $phase_i$ is the phase difference between before and after PA excitation; and $\overline{phase}$ is the average phase difference.

In Fig. 1(c) and (d), we can see strong random noise fluctuation at low-intensity pixels (i.e., above the sample surface and deep in the sample). Random noise disturbed the PA detection. Here, only pixels with sufficient OCT signal intensity were adopted for PA detection. For each A-line of the OCT signal, an edge detection algorithm was used to identify the sample surface, and then a threshold segmentation algorithm was used to extract pixels in the sample with sufficient intensity. We set the phase difference of those unselected (low intensity) pixels to zero and the results were shown in Fig. 1(e) and (f) (corresponding to (c) and (d) respectively). The STD values in (e) are 0.13 rad (blue curve) and 2.04 rad (red curve). PA vibration induced significant phase variance. The STD values in (f) are 0.15 rad (blue curve) and 0.17 rad (red curve). Agar cannot absorb excitation light and generate PA vibration. Thus, there is no significant difference between the two curves in (f).

2.3. OCT and PAM system

A schematic of the OCT-PAM dual-mode system setup is given in Fig. 2. A superluminescent diode (SLD, D-840-HP, Superlum) with 840 nm centre wavelength and 50 nm bandwidth is employed as the light source of the SDOCT (orange beam in Fig. 2). A fibre-based Michelson interferometer was assembled using a circulator (CIR) and a 90:10 fibre coupler (TW850R2A2, Thorlabs), which split the beam into sample arm and reference arm. The interference spectrum is captured by a custom-made high-speed spectrometer composed of a collimating lens, a transmission grating, a focal lens, and a line-scan camera (spL2048–140 km, Basler). The maximum rate of the camera is 70 kHz. A passively Q-switched pulsed laser (MCA-532–2.5–060, RealLight TECH. Ltd, China) operating at 532 nm (green beam in Fig. 2) was used

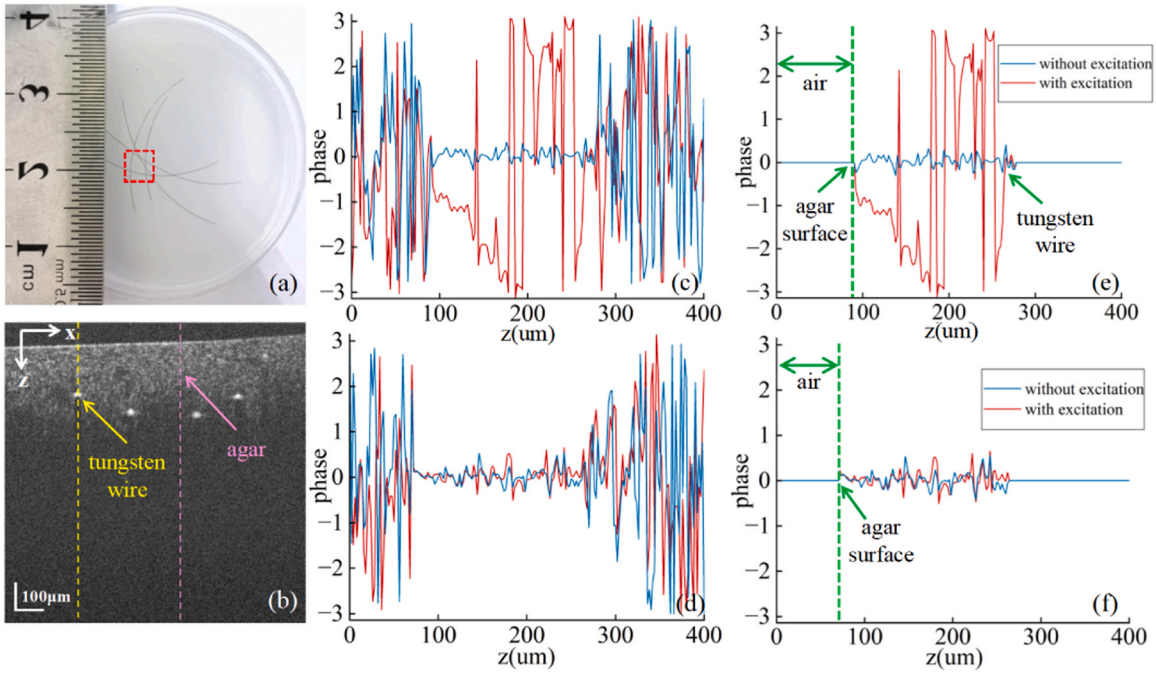

Fig. 1. Acoustic wave propagation introduces phase variance in SDOCT signal. (a) photograph of tungsten wire embedded in the agar mixture of intralipid; (b) the cross-section structural image of OCT B-scan; (c) phase difference acquired with and without PA excitation (focused on the tungsten wire, dashed yellow line in (b)); (d) phase difference with and without the excitation (focused on the agar area, dashed pink line in (b)); (e) phase difference curves corresponding to (c) after random phase noise removal; (f) phase difference curves corresponding to (d) after random noise removal.

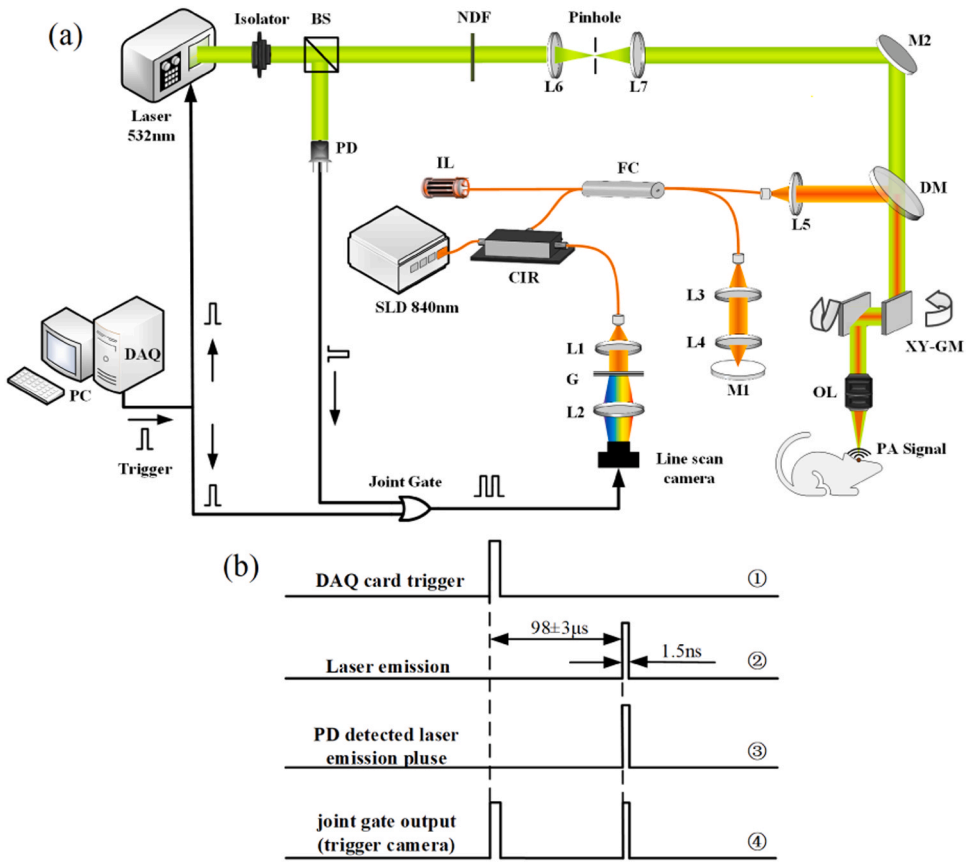

Fig. 2. OCT-PAM dual-mode system. (a) the schematic of the OCT-PAM dual-mode system; (b) the flow chart of the synchronization process between SDOCT and PA excitation. IL, indicator light; SLD, superluminescent diode; CIR, circulator; FC, fibre coupler; M1 and M2, mirror; L1–L7, lens; OL, object lens; DM, dichroic mirror; G, grating; NDF, neutral density filter; XY-GM, XY-galvanometer mirror; BS, beam splitter; PD, photodiode.

to excite the PA signal. The pulse width is 1.5 ns with a maximum pulse repetition frequency (PRF) of 2.5 kHz. The emitted light passed through an optical isolator first and then shaped by a beam-shaping module consisting of L6, L7 and pinholes in Fig. 2. To adjust the intensity of the excitation light, a neutral density filter (NDF) was placed in front of the module. The pulsed laser and the OCT light are combined by a dichromatic mirror (DMSP650, Thorlabs) to achieve coaxial propagation. The combined beam was then directed onto the sample by an optical probe arm containing an X-Y scanner and an objective lens. (NA=0.1, PLN4 ×, Olympus).

In PAM imaging, the PA excitation source and the line scan camera worked in external trigger mode. The flow chart of the synchronization process between SDOCT and PA excitation is shown in Fig. 2(b). To detect PA signals, two OCT A-lines are required for PA vibration-induced phase difference calculation. At each point on the sample, the DAQ card (PCI 6713, National Instrument) generated a pulse to trigger the PA excitation source (① in Fig. 2(b)). Simultaneously, the pulse also served as an input of a joint (OR) gate (in Fig. 2(a)). The PA excitation source received the trigger pulse and generated a laser pulse (② in Fig. 2(b)). There was a certain time delay between the input electric pulse trigger and the output laser pulse. The delay time was approximately 98±3μs. A photodiode (SM05PD2A, Thorlabs) monitored the laser emission and generated another electric pulse (③ in Fig. 2(b)). The pulse (③) is the other input of the joint gate. The output of the joint gate (④ in Fig. 2(b)) contains two pulses (① + ③), which were used to trigger the line scan camera acquisition. Thus, each PA excitation corresponds to two interference spectrum acquisitions (before and after the excitation). The time interval between the two spectrum acquisitions is mainly determined by the time delay in the PA excitation laser (② in Fig. 2(b), 98±3μs) since the pulse width of the excitation laser is ~1.5 ns and the response time (rise time) of the photodiode is ~1 ns.

3. Results

3.1. Resolution of the system

To evaluate the OCT axial resolution, a planar mirror was imaged as the standard sample. The full width at half maximum (FWHM) of the OCT signal (Fig. 3(a)) determined the axial resolution. The axial resolution of OCT was measured to be ~9μm. The lateral resolution of OCT and PAM were measured by imaging the sharp edge of a blade. In Fig. 3 (b) and Fig. 3(c), the black points are the raw data from a one-dimensional scan across the sample edge. Then to derive the line spread function (LSF), the edge spread function (ESF) was acquired and fitted. The lateral resolution was considered to be the FWHM of the LSF. And the lateral resolution of OCT and PAM was about 7μm and 6μm respectively (Fig. 3(b) and (c)).

3.2. Phantom study

We imaged a phantom with carbon fibers (~7 μm) embedded in scattering gel to evaluate the performance of the proposed system. The scattering gel was prepared by mixing the agar with a 1 % intralipid, which produced a scatter background similar to that of tissue. The frequency of the synchronization pulse train (from the DAQ card) is set at 2000 Hz. At each point of the phantom, interference spectrums were acquired before (SP_1) and after (SP_2) the PA excitation. Then, FFT was performed on the two spectrums. The amplitude of FFT(SP_1) was used to build an OCT structural image. The phase difference between FFT(SP_1) and FFT(SP_2) was used for PAM imaging. We acquired 400 × 400 (X×Y)

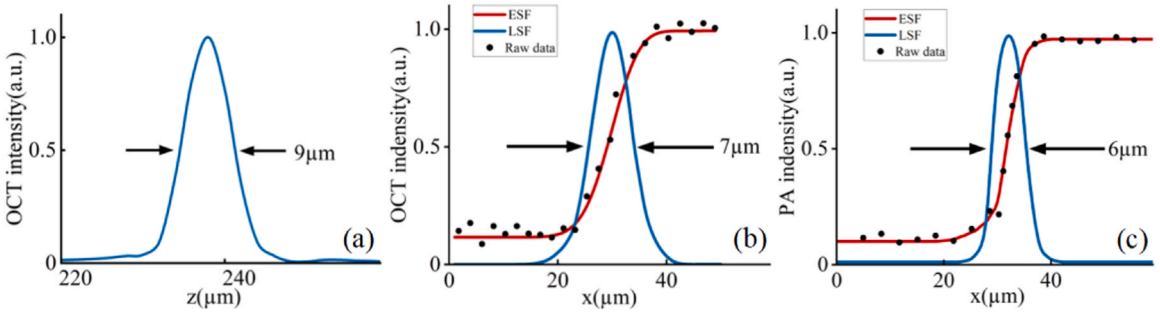

Fig. 3. Resolution of the OCT-PAM system. (a) axial resolution of SDOCT; (b) lateral resolution of SDOCT; (c) lateral resolution of PAM.

points covering 5 × 5 mm^2. The acquisition is ~100 s. The speed of the imaging process is mainly limited by the excitation laser pulse repetition rate. Fig. 4(a) shows the *en-face* maximum intensity projection (MIP) image of OCT, and The B-scan of the cross-section corresponding to the dashed line in Fig. 4(a) is shown in Fig. 4(b). And Fig. 4(c) shows the *en-face* PAM image. Compared to Fig. 4(a) and (c), the carbon fibers distribution acquired by the two imaging modalities corresponds well. In OCT images, some carbon fibers are blurry or even absent (Fig. 4(a) and (c) white arrows). This is because of the focus mismatch between the detecting beam of OCT and the excitation beam of PAM. The two beams are generated from different light sources with different wavelengths. The two beams were combined by a dichroic mirror and the combined coaxial beam was then focused onto the sample using a larger NA objective lens. Thus, it is difficult to realize the perfect coincidence of the two focuses. During the experiment, we focused the PAM excitation beam on the carbon fibers to achieve optimal PAM images, which may sacrifice the imaging quality of OCT.

We also conducted imaging on another sample exhibiting branching patterns. An asparagus leaf was immersed in black ink for over 5 h, followed by rinsing off the residual ink (which did not infiltrate the leaf veins) with clear water. Subsequently, the prepared sample was embedded in a scattering medium and subjected to imaging. The scattering medium was made in the same way as described above. An appropriate location on the sample was chosen for imaging (Fig. 5(a)), and the field of view was 4×4 mm^2. The corresponding PAM result for the selected area is presented in Fig. 5(b), and an *en-face* MIP OCT image is shown in Fig. 5(c). Fig. 5(d) displays the OCT B-scan cross-sectional image matched with the white dashed line in Fig. 5(c). These results further demonstrated the capability of our imaging system.

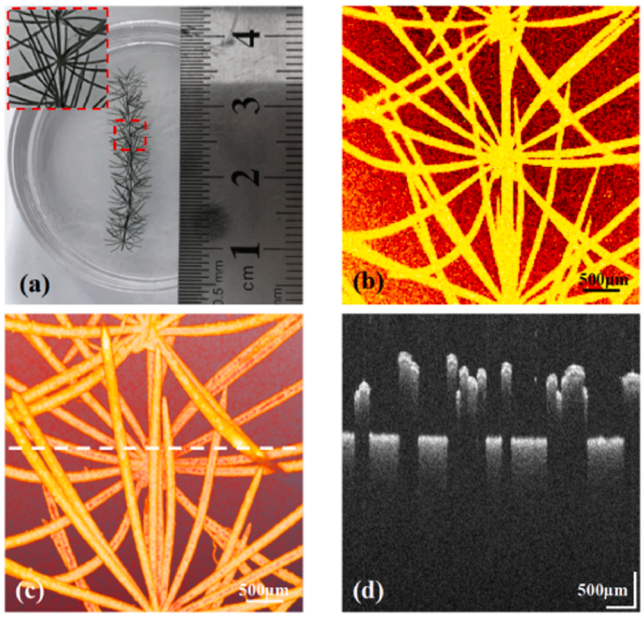

Fig. 5. Asparagus leaf imaging with the dual-mode system. (a) photograph of asparagus leaf embedded in the agar mixture of intralipid; (b) PAM result for the selected area; (c) *en-face* MIP OCT image; (d) the cross-sectional OCT B-scan image corresponding to the white dotted line in (c).

3.3. OCT-PAM dual-mode imaging on human hair phantom

To demonstrate the advantage of dual-mode imaging, we imaged a human hair phantom using the proposed system. Two black hairs and two white hairs were embedded in the agar mixture of intralipid. Fig. 6(a) shows the photograph of the phantom. An appropriate location on the sample was chosen for imaging, and the field of view was 4×4 mm^2. Fig. 6(b) shows the PAM result. We can see that black hair absorbs PA excitation, which can be visualized by PAM. In contrast, white hairs

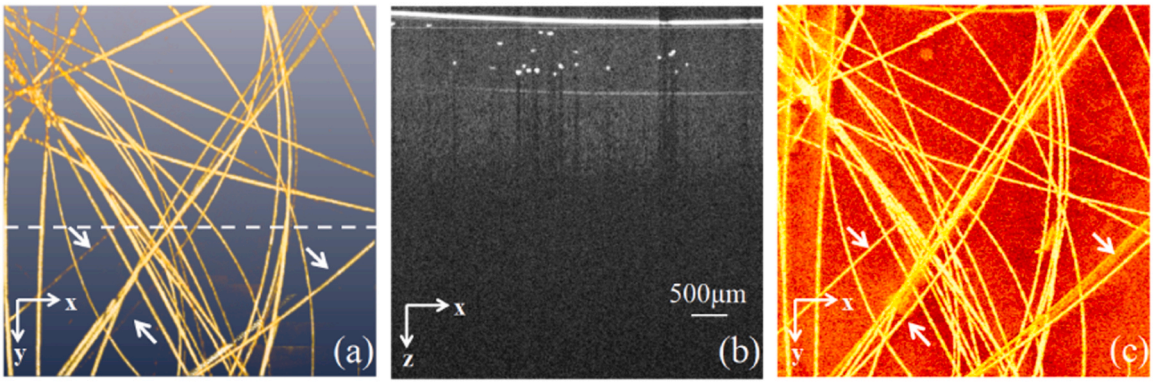

Fig. 4. The dual-mode imaging results of carbon fibers. (a) the *en-face* MIP image of OCT; (b) the cross-sectional OCT B-scan image corresponding to the dashed line in (a); (c) the PAM result.

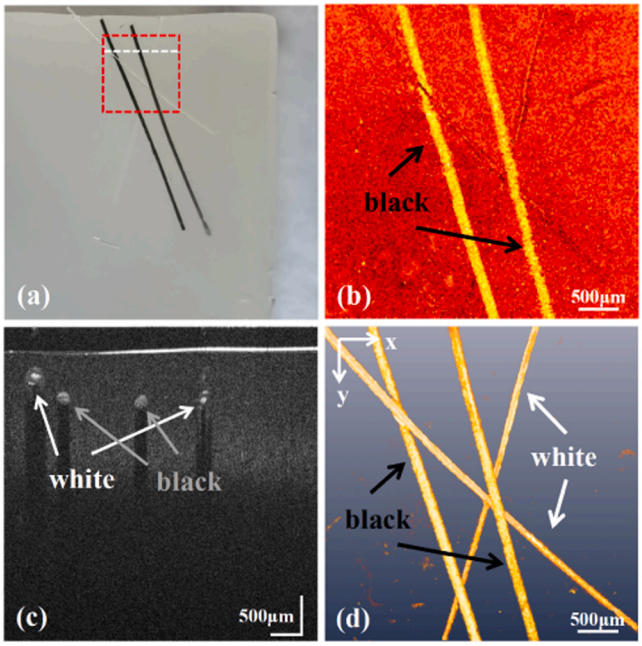

Fig. 6. Human hair phantom imaging with the dual-mode system. (a) photograph of a human hair phantom; (b) the PAM result; (c) cross-sectional OCT B-scan image corresponding to the white dotted line in (a); (d) *en-face* MIP OCT image.

absorb little PA excitation and are invisible on PAM. Fig. 6(c) shows the OCT B-scan image matched with the white dashed line in Fig. 6(a), and an *en-face* MIP OCT image is displayed in Fig. 6(d). OCT is based on light backscatter for imaging. Backscatter is mainly determined by refractive index difference in the sample. Black hair and white hair have similar refractive index and are different from the agar. Thus, both black and white hairs were visualized in OCT. The experiment demonstrated that OCT-PAM dual-mode can provide complementary contrast, i.e., OCT for backscattering and PAM for absorption.

3.4. Imaging of rat cortex vasculature in vivo

We also imaged the cortex vasculature of rats *in vivo*. Male Sprague-Dawley (SD) rats about 3 months of age, weighing 250 ~ 280 g each, were selected for the experiment. All experimental operations were carried out in conformity with the Guide for the Care and Use of Laboratory Animals regulated by the National Institutes of Health and the standards of the Northeastern University Animal Ethics Committee. All possible measures were taken to minimise the suffering of animals and to minimise the amount of animals used. Sodium pentobarbital (3 %, 5 mg/100 g, IP) was used to induce surgical anaesthesia before the experiment. A thermostatic blanket was used to keep the body temperature of the animals at 36.8°C during the experiment. The anaesthetised rats were immobilised on the stereotaxic apparatus (ST-5ND-C) with a nose clip and ear rods. The fur on the rats' heads was removed using a depilatory cream, after which the skin was washed clean with 0.9 % physiological saline solution. The rat scalp was incised along the cranial midline, exposing the interparietal bone. The subcutaneous tissue and the periosteum were subsequently cleared. A cranial window measuring 5 × 5 mm^2 was created in the left parietal cortex, situated 0.5 mm lateral from the sagittal suture and 0.5 mm posterior from the bregma. After surgery, the rats were placed on the imaging platform for data acquisition.

For OCTA imaging, the scan protocol is similar to our previous publication [44]. In brief, four B-scans were performed repeatedly at each position (Y direction). Each B-scan consists of 400 A-lines acquired with the line scan speed at 25,000 Hz. The repeated B-scans were performed at 400 positions. The imaging area is 4 mm×4 mm (X×Y) mm. Fig. 7(a) illustrates a representative OCT B-scan structural image of the rat cortex, corresponding to the white dashed line in Fig. 7(c). Using Eq. (3), the blood flow signal was extracted from the repeated B-scans (Fig. 7(b)). Fig. 7(c) shows the achieved OCTA image. The optical energy irradiated to the sample during OCT imaging is about 3 mW, which is within the safe range of near-infrared light required by American National Standards Institute (ANSI) standards. As for the PAM imaging, the data acquisition is the same as the protocol described in Section 3.2. Briefly, interference spectrums were acquired before and after the PA excitation. The phase change between the two A-scans was used for PA signal extraction. Fig. 7(d) shows the PAM imaging result which consists of 400×400 pixels (corresponding to 4 mm×4 mm imaging area). In this study, the energy of each excitation pulse for *in vivo* imaging was 250nJ, corresponding to a surface fluence of about 3 mJ/cm^2 calculated by Ref. [41]. The surface fluence is below the single-pulse limit of 20 mJ/cm^2, established by the ANSI.

In the OCTA image (Fig. 7(c)), the large vessels' intensity is not identical, i.e. the centre of the blood vessel has a higher intensity than the border (green arrows in (c)). OCTA is a method based upon the principle of contrast imaging utilising motion. For large vessels, the flow of the centre is fast, corresponding to the high OCTA intensity. A comparison of Fig. 7(c) and (d) reveals that the blood vessel diameter of PAM is slightly larger than OCTA, especially at some vascular branches (blue arrows in (c) and (d)). Eventually, OCTA extracts blood cell motion to visualize blood vessels. There is a certain speed limitation that low-speed motion is undetectable by OCTA. Thus, the visualized vessel diameter decrease in OCTA is attributed to the low-velocity blood flow at the vessel border. On the other hand, PAM imaging is founded upon the phenomenon of red blood cells' absorption of the excitation light. The distribution of red blood cells is the primary determinant of this phenomenon, regardless of their state of flow [42]. Thus, the visualized blood vessel in PAM is closer to the real diameter than OCTA.

3.5. Blood perfusion evaluation of rat cortex by OCT-PAM dual-mode imaging

To demonstrate the advantage of dual-mode imaging, we imaged rat

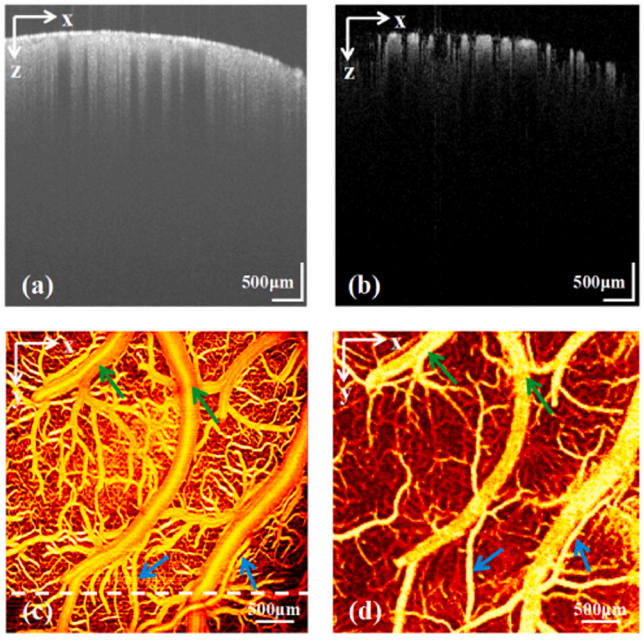

Fig. 7. Dual-mode imaging results of the rat cortical vasculature. (a) OCT B-scan structure image (white dashed line in (c)); (b) OCTA result of blood flow signal; (c) *en-face* OCTA image; (d) PAM image.

cortex vasculature of an animal model called bilateral common carotid arteries occlusion (BCCAo) [43]. Firstly, the vasculature of the rat cortex was imaged by OCT (Fig. 8(a)) and PAM (Fig. 8(c)) as a baseline. Then, bilateral common carotid arteries of rats were occluded (detail operation, please see reference [43]). After the occlusion, dual-mode imaging was performed immediately. Fig. 8(b) and Fig. 8(d) show the OCTA and PAM results correspondingly. The experiment was conducted on six rats. To quantify vascular parameters, Fig. 8(a-d) was binarized by the previously proposed "locally adaptive region growing" algorithm [44], and the results are shown in Fig. 8(e-h). Based on the binarized image, three vascular parameters were quantified to evaluate the blood flow status, including vascular perfusion density (VPD), vascular diameter (VD) and vascular length (VL) [46]. VPD was defined as the ratio of "the number of blood vessel pixels" to "the total number of pixels in the angiogram". Fig. 8(i-l) are the VPD maps, in which each pixel value represents the VPD at the local region around the point. The distance transformation was performed on the binarized images to obtain the vascular skeleton diagrams (Fig. 8(m-p)). Each pixel value in the vascular skeleton diagrams represents the blood vessel's radius (the unit is μm), and the VD can be obtained by multiplying that value by 2. VL is the length of the vascular skeleton. Fig. 8(q-s) exhibits the statistics of the three parameters achieved from OCTA and PAM images before and after the occlusion.

In Fig. 8(a) and (c), we can see that both OCTA and PAM can detect abundant blood vessels before the occlusion. After the occlusion, only large veins can be visualized by OCTA (Fig. 8(b)), and the VPD and VL decreased by 60.1 % and 58.6 %, respectively (Fig. 8(q) and (s)). Meanwhile, the massive reduction of small vessels led to a 16 % increase in VD (Fig. 8(r)). For PAM, although a few small vessels become undetectable after the occlusion (Fig. 8(d)), most blood vessels can still be captured, and the three statistical parameters changed slightly. The VD increased 1 %, and the VPD and VL decreased by 8.2 % and 8.8 %, respectively (Fig. 8(q-s)). The sudden occlusion of the bilateral common carotid arteries ceased the blood supply on the cortex and caused blood flow in arteries to stop. Only part of the vein return is maintained in the cortex. OCTA detected these veins with blood flow since OCTA is a technique based on motion contrast for imaging. Red blood cells are still retained for those flow-ceased vessels and can be detected by PAM. Blood flow status can be evaluated when combined with the two imaging modalities. Blood flow status is essential for mechanical studies for blood supply-related diseases (such as ischemic stroke). The proposed OCT-PAM dual-mode system has the potential to promote related research.

4. Discussion

In our previous work [34], we proposed an interference contrast reduction method for PA detection. The method focused on the interference between the sample surface and the reference arm. The spectral interference contrast decreases because of the surface vibration induced by PA excitation. Generally, the sample's surface is rough, and the reflection is weak. Thus, the sample requires a thin layer of water (or oil) film, which can provide sufficient reflection and remove the influence of speckles [31]. We compared the performance of the two methods (previous and current) by imaging the vasculature of rat cortex *in vivo*. The rat operation is the same as the procedure described in Section 3.4.

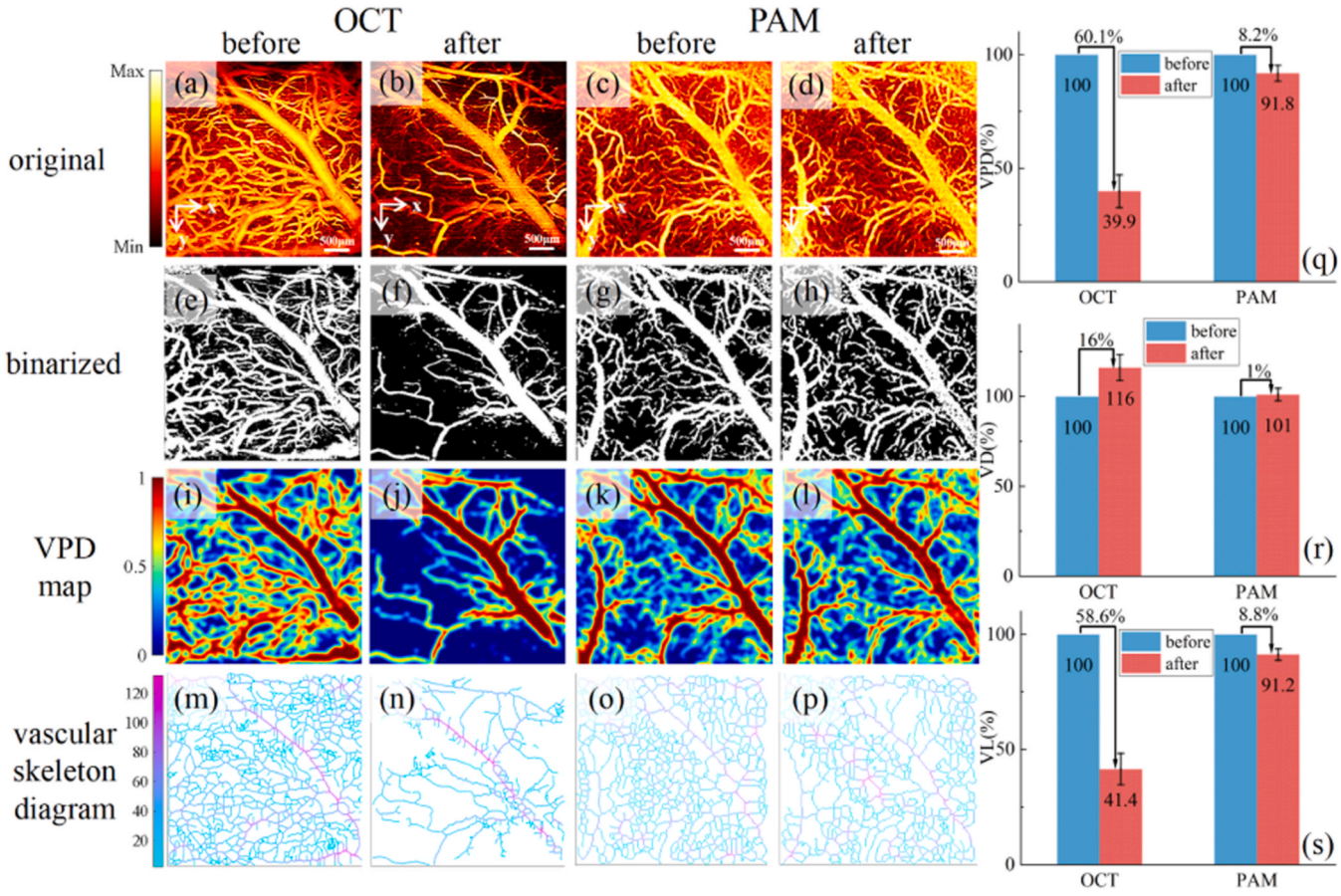

Fig. 8. Quantified dual-mode imaging results of BCCAo model (n=6). (a) *en-face* OCTA image before occlusion; (b) *en-face* OCTA image after occlusion; (c) PAM image before occlusion; (d) PAM image after occlusion; (e-h) binarized angiography images corresponding to (a-d); (i-l) VPD maps corresponding to (a-d); (m-p) vascular skeleton diagrams corresponding to (a-d); (q) comparison of VPD before and after occlusion in OCT and PAM; (r) comparison of VD before and after occlusion in OCT and PAM; (s) comparison of VL before and after occlusion in OCT and PAM.

A thin water film was built on the sample. PAM imaging was performed using the previous method, and the result is shown in Fig. 9(a). Then, the water film was removed from the sample. Using the current method, we imaged the same area on the rat cortex (Fig. 9(b)). The two results were acquired with the same PA excitation energy. Compared to the two results, we can see that the current method visualized more blood vessels. The performance improvement originated from parallel detection (or multi-layer detection). Only interference induced from the water film surface (single-layer) is considered for the previous method. In contrast, the current method calculated the STD of phase difference among multiple pixels (corresponding to multi-layers). Thus, the current method is more sensitive to PA vibration than the previous method.

The proposed method uses the STD of phase difference to detect the PA signal. On the other hand, blood flow also can cause phase change between repeated A-scans, i.e., Doppler OCT. In a sense, Doppler-induced phase difference is helpful for blood vessel detection. However, the help is almost negligible since PAM concentrates more on small vessels. For OCT A-lines containing small vessels, blood flow only presents at a few pixels and affects little on STD calculation (Eq. (10)). For large vessels, the flow velocity is fast, and the diameter is big. Theoretically, the Doppler phase difference can slightly increase the STD value. Considering the PA signal of large vessels is strong, the STD increase caused by blood flow also has little effect. Another problem concerning the proposed method is phase wrapping, which is an inherent problem for phase-related techniques. Eventually, the proposed method measures the displacement caused by PA vibration for imaging. The displacement corresponds to the phase difference. When the displacement exceeds a certain threshold, phase wrapping occurs because the value of phase was confined within [-π π]. Thus, phase wrapping deteriorates the PA vibration detection since it limits the maximum measurable displacement. Furthermore, phase wrapping destroyed the linear mapping between the displacement and the phase difference, which obstructs the quantitative measurement of the PA signal. Proper phase unwrapping algorithms are possible solutions to improve the performance of the proposed method. For the proposed method, SDOCT is utilized to detect phase differences induced by PA vibration. Thus, the phase stability of SDOCT is crucial for detection. Using a phantom of agar mixture with intralipid as the sample, 1000 A-scans were acquired by SDOCT. The phase difference between the adjacent two A-lines was calculated. The mean STD of phase difference is about 0.15 rad. Using a tungsten wire phantom as a sample, the mean STD of phase difference is about 2.09 rad (1000 times excitation). Therefore, the phase stability of SDOCT is sufficient for PA detection.

Absorption and Scattering are two basic forms of interaction between light and tissue, represented by PAM and OCT, respectively [45]. PAM can offer abundant and specific molecular-level absorption contrast at the μm scale [15], which renders it an invaluable tool for biomedical research. Unlike PAM, the contrast provided by OCT is generated through the scattering of light within the tissue microstructure. In addition to the initial structural imaging, OCT has developed several extended functions, including DOCT [4], OCTA [6], and OCT attenuation imaging (OCT-AI) [46], etc. The capacity of OCT and PAM to offer complementary information renders them the ideal modalities for multimodal imaging systems. The integrated system provides a powerful tool for the research of diseases in the vascular system such as ischemia, bleeding, and vascular obstructions [19,47]. Meanwhile, OCT and PAM systems help to diagnose brain diseases such as stroke and oedema by providing detailed vascular structure and subcellular features [48,49]. On the other hand, PAM has a significant advantage in quantitative oxygen saturation studies and, when combined with Doppler OCT blood flow velocity measurements, will facilitate physiopathological studies of angiogenesis and inflammatory responses. In a word, as a compound imaging method, OCT-PAM imaging can provide more comprehensive information, play a key role in disease monitoring, diagnosis and treatment, and have broad prospects in biomedical imaging.

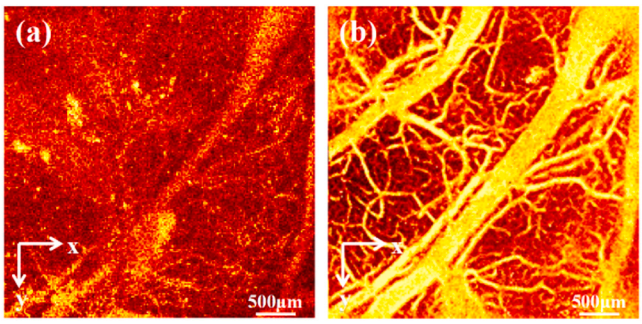

Fig. 9. PAM imaging of rat cortical vasculature with different methods. (a) the result of the previous spectral interference contrast reduction method; (b) the result of the proposed phase difference method.

Both OCT and PAM are optical imaging and require light sources and signal detection units. Traditional PA imaging uses ultrasonic transducers, and the probe needs physical contact with the sample, which blocks the detection light of OCT. Non-contact PA detection usually uses an optical detection method to replace the traditional ultrasonic transducer, which does not need to contact the sample and simplifies the combination with OCT [31]. In most OCT-PAM dual-mode imaging systems, the probe terminal usually requires three beams coupling, including OCT detection light, PA excitation light, and PA detection light. Multiple optical coupling increases the difficulty of optical path adjustment, and at the same time, it causes light energy loss due to coupling efficiency. Moreover, the OCT and PAM of the OCT-PAM dual-mode imaging system need corresponding detection units respectively, and the dual detection units also increase the complexity of the system [50]. In this paper, we proposed a probe fusion non-contact OCT-PAM dual-mode imaging system. At the probe terminal, only two light channels (PA excitation light and OCT probe light) are coupled, which further simplifies the system and reduces the difficulty of system adjustment. SDOCT was used to detect the phase change of the sample resulting from the PA vibration, without the need for a separate unit for PA signal detection. Importantly, our method analyzed the OCT signal within the sample to detect the PA signal, needless to create a water film on the sample surface [34], which realized complete non-contact imaging. This is particularly beneficial in disease examination, as it minimizes the potential risk of infection.

In OCT-PAM systems, the lateral resolution of both modes is contingent on the optical focusing, which allows a high lateral resolution (~10μm) [51]. The OCT axial resolution is dependent upon the spectral bandwidth of the light source (~several microns). In the case of traditional transducer-based PAM, the axial resolution is contingent upon the bandwidth of the detector and ultrasound attenuation, usually several tens of microns [42]. For the proposed SDOCT detection-based PAM, the axial resolution is poor because the exposure time of each SDOCT A-scan is tens of microseconds while the velocity of ultrasound in tissue is ~1500 m/s. Theoretically, the axial resolution of PAM can be enhanced simply by reducing the exposure time of SDOCT. However, this approach is not practical since SDOCT can't provide a sufficient SNR for imaging with ultrashort exposure time. In 2019, Matan et al. proposed a noncontact method of PA imaging employing a laser speckle contrast analysis [33]. The axial resolution was enhanced by a gradual alteration of the exposure start time. This protocol can be ported to our method. However, the operation increases acquisition time. For the dual-mode system, OCT is capable of providing excellent axial resolution, which can partially compensate for the drawback of poor axial resolution in PAM.

5. Conclusions

In summary, we proposed a probe fusion all-optic OCT-PAM dual-mode imaging system for biomedical imaging. Here, the PA signal was

detected by SDOCT, i.e. SDOCT serves as the detection unit of PAM. Thus, the dual-mode imaging system consists of a standard SDOCT and a PA excitation laser. Compared with other OCT-PAM systems, the proposed system is simple in construction. Furthermore, the system realized total non-contact detection for both of the two imaging modalities, which is critical for biomedical imaging. The imaging capability of the system was proved by imaging phantoms and cerebral cortex vasculature of rats *in vivo*. The proposed system facilitates the combination of OCT and PAM and has a rosy prospect in biomedical applications. More efforts are underway to improve the performance of the system.

CRediT authorship contribution statement

Huiwen Jiang: Validation. **Ben Xiang:** Software. **Zhenhe Ma:** Writing – review & editing, Supervision, Resources, Project administration, Investigation. **Ning Ding:** Writing – review & editing, Writing – original draft, Visualization, Validation, Software, Methodology, Investigation, Formal analysis, Data curation, Conceptualization. **Yao Yu:** Writing – review & editing, Funding acquisition. **Cheng Ji:** Resources. **Jian Liu:** Supervision. **Yanqiu Yang:** Methodology. **Yi Wang:** Funding acquisition. **Yuqian Zhao:** Funding acquisition. **Jingmin Luan:** Software.

Declaration of Competing Interest

The authors declare that they have no known competing financial interests or personal relationships that could have appeared to influence the work reported in this paper.

Data availability

Data will be made available on request.

Acknowledgements

Funding: This work was supported by the National Natural Science Foundation of China [grant numbers 62075037, 62301137]; and the Fundamental Research Funds for the Central Universities [grant number 2022GFZD013].

References

[1] A. Fercher, W. Drexler, C. Hitzenberger, T. Lasser, Optical coherence tomography—principles and applications, Rep. Prog. Phys. 66 (2003) 239.
[2] D. Huang, E.A. Swanson, C.P. Lin, J.S. Schuman, W.G. Stinson, W. Chang, M. R. Hee, T. Flotte, K. Gregory, C.A. Puliafito, J.G. Fujimoto, Optical coherence tomography, Science 254 (5035) (1991) 1178–1181.
[3] M. Wojtkowski, V.J. Srinivasan, T.H. Ko, J.G. Fujimoto, A. Kowalczyk, J.S. Duker, Ultrahigh-resolution, high-speed, Fourier domain optical coherence tomography and methods for dispersion compensation, Opt. Express 12 (11) (2004) 2404–2422.
[4] R.A. Leitgeb, R.M. Werkmeister, C. Blatter, L. Schmetterer, Doppler optical coherence tomography, Prog. Retin. Eye Res. 41 (2014) 26–43.
[5] X.Y. Liu, L.Q. Jiang, M.Y. Ke, I.A. Sigal, J. Chua, Q.V. Hoang, A.W.I. Chia, R. P. Najjar, B.Y. Tan, J.C.Y. Cheong, V. Bellemo, R.S. Chong, M.J.A. Girard, M. Ang, M.Y. Liu, G. Garhöfer, V.A. Barathi, S.M. Saw, M. Villiger, L. Schmetterer, Posterior scleral birefringence measured by triple-input polarization-sensitive imaging as a biomarker of myopia progression, Nat. Biomed. Eng. 7 (8) (2023) 986.
[6] A. Zhang, Q. Zhang, C.L. Chen, R. Wang, Methods and algorithms for optical coherence tomography-based angiography: a review and comparison, J. Biomed. Opt. 20 (10) (2015) 100901.
[7] V. Ntziachristos, Going deeper than microscopy: the optical imaging frontier in biology, Nat. Methods 7 (8) (2010) 603–614.
[8] P. Beard, Biomedical photoacoustic imaging, Interface Focus 1 (4) (2011) 602–631.
[9] Z.L. Tan, Y.F. Liao, Y.B. Wu, Z.L. Tang, R.K.K. Wang, Photoacoustic microscopy achieved by microcavity synchronous parallel acquisition technique, Opt. Express 20 (5) (2012) 5802–5808.
[10] J.M. Yang, C. Favazza, R.M. Chen, J.J. Yao, X. Cai, K. Maslov, Q.F. Zhou, K. K. Shung, L.H.V. Wang, Simultaneous functional photoacoustic and ultrasonic endoscopy of internal organs, Nat. Med. 18 (8) (2012) 1297.
[11] J. Yao, L. Wang, J.-M. Yang, K.I. Maslov, T.T.W. Wong, L. Li, C.-H. Huang, J. Zou, L.V. Wang, High-speed label-free functional photoacoustic microscopy of mouse brain in action, Nat. Methods 12 (5) (2015) 407–410.
[12] L.H.V. Wang, J.J. Yao, A practical guide to photoacoustic tomography in the life sciences, Nat. Methods 13 (8) (2016) 627–638.
[13] S. Jeon, J. Kim, D. Lee, J.W. Baik, C. Kim, Review on practical photoacoustic microscopy, Photoacoustics 15 (2019) 100141.
[14] S. Cheng, Y. Zhou, J. Chen, H. Li, L. Wang, P. Lai, High-resolution photoacoustic microscopy with deep penetration through learning, Photoacoustics 25 (2022) 100314.
[15] J.S. Zhou, W. Wang, L.L. Jing, S.L. Chen, Dual-modal imaging with non-contact photoacoustic microscopy and fluorescence microscopy, Opt. Lett. 46 (5) (2021) 997–1000.
[16] W. Qiao, Z.J. Chen, All-optically integrated photoacoustic and optical coherence tomography: a review, J. Innov. Opt. Heal Sci. 10 (4) (2017).
[17] S.L. Jiao, Z.X. Xie, H.F. Zhang, C.A. Puliafito, Simultaneous multimodal imaging with integrated photoacoustic microscopy and optical coherence tomography, Opt. Lett. 34 (19) (2009) 2961–2963.
[18] Z. Chen, E. Rank, K.M. Meiburger, C. Sinz, A. Hodul, E. Zhang, E. Hoover, M. Minneman, J. Ensher, P.C. Beard, H. Kittler, R.A. Leitgeb, W. Drexler, M.Y. Liu, Non-invasive multimodal optical coherence and photoacoustic tomography for human skin imaging, Sci. Rep. -Uk 7 (2017).
[19] Z. Ma, S. Luo, M. Yu, J. Liu, Y. Zhao, Y. Yu, J. Lv, X. Zhang, Y. Wang, Assessment of microvasculature flow state with a high speed all-optic dual-modal system of optical coherence tomography and photoacoustic imaging, Biomed. Opt. Express 9 (12) (2018) 6103–6115.
[20] V. Ntziachristos, J.S. Yoo, G.M. van Dam, Current concepts and future perspectives on surgical optical imaging in cancer, J. Biomed. Opt. 15 (6) (2010).
[21] G. Rousseau, B. Gauthier, A. Blouin, J.P. Monchalin, Non-contact biomedical photoacoustic and ultrasound imaging, J. Biomed. Opt. 17 (6) (2012).
[22] E. Leiss-Holzinger, J. Bauer-Marschallinger, A. Hochreiner, P. Hollinger, T. Berer, Dual modality noncontact photoacoustic and spectral domain OCT imaging, Ultrason. Imaging 38 (1) (2016) 19–31.
[23] S.A. Carp, A. Guerra, S.Q. Duque, V. Venugopalan, Optoacoustic imaging using interferometric measurement of surface displacement, Appl. Phys. Lett. 85 (23) (2004) 5772–5774.
[24] S.A. Carp, V. Venugopalan, Optoacoustic imaging based on the interferometric measurement of surface displacement, J. Biomed. Opt. 12 (6) (2007).
[25] A. Hochreiner, J. Bauer-Marschallinger, P. Burgholzer, B. Jakoby, T. Berer, Non-contact photoacoustic imaging using a fiber based interferometer with optical amplification, Biomed. Opt. Express 4 (11) (2013) 2322–2331.
[26] G. Rousseau, A. Blouin, J.P. Monchalin, Non-contact photoacoustic tomography and ultrasonography for tissue imaging, Biomed. Opt. Express 3 (1) (2012) 16–25.
[27] E. Zhang, J. Laufer, P. Beard, Backward-mode multiwavelength photoacoustic scanner using a planar Fabry-Perot polymer film ultrasound sensor for high-resolution three-dimensional imaging of biological tissues, Appl. Opt. 47 (4) (2008) 561–577.
[28] M. Liu, Z. Chen, B. Zabihian, C. Sinz, E. Zhang, P.C. Beard, L. Ginner, E. Hoover, M. P. Minneman, R.A. Leitgeb, H. Kittler, W. Drexler, Combined multi-modal photoacoustic tomography, optical coherence tomography (OCT) and OCT angiography system with an articulated probe for in vivo human skin structure and vasculature imaging, Biomed. Opt. Express 7 (9) (2016) 3390–3402.
[29] J. Eom, J.G. Shin, S. Park, S. Rim, B.H. Lee, An all-fiber-optic combined system of noncontact photoacoustic tomography and optical coherence tomography, Sensors-Basel 16 (5) (2016) 734.
[30] J. Lu, Y.Z. Gao, Z.H. Ma, H.X. Zhou, R.K.K. Wang, Y. Wang, photoacoustic imaging of blood vessels using a homodyne interferometer with zero-crossing triggering, J. Biomed. Opt. 22 (3) (2017).
[31] Y. Wang, C. Li, R.K. Wang, Noncontact photoacoustic imaging achieved by using a low-coherence interferometer as the acoustic detector, Opt. Lett. 36 (20) (2011) 3975–3977.
[32] C. Blatter, B. Grajciar, P. Zou, W. Wieser, A.J. Verhoef, R. Huber, R.A. Leitgeb, Intrasweep phase-sensitive optical coherence tomography for noncontact optical photoacoustic imaging, Opt. Lett. 37 (21) (2012) 4368–4370.
[33] M. Benyaniin, H. Genish, R. Califa, A. Schwartz, Z. Zalevsky, N. Ozana, Non-contact photoacoustic imaging using laser speckle contrast analysis, Opt. Lett. 44 (12) (2019) 3110–3113.
[34] Z.H. Ma, N. Ding, Z. Li, K.L. Zhu, A. Li, Z.H. Lin, Y. Wang, Y.Q. Zhao, Y. Yu, J. M. Luan, X. Zhu, J. Liu, Spectral interference contrast based non-contact photoacoustic microscopy realized by SDOCT, Opt. Lett. 47 (11) (2022) 2895–2898.
[35] R.K. Wang, S.L. Jacques, Z. Ma, S. Hurst, S.R. Hanson, A. Gruber, Three dimensional optical angiography, Opt. Express 15 (7) (2007) 4083–4097.
[36] Z. Chen, T.E. Milner, S. Srinivas, X. Wang, A. Malekafzali, M.J.C. van Gemert, J. S. Nelson, Noninvasive imaging of in vivo blood flow velocity using optical Doppler tomography, Opt. Lett. 22 (14) (1997) 1119–1121.
[37] T. Vu, P. Klippel, A.J. Canning, C. Ma, H. Zhang, L.A. Kasatkina, Y. Tang, J. Xia, V. V. Verkhusha, T. Vo-Dinh, Y. Jing, J. Yao, On the importance of low-frequency signals in functional and molecular photoacoustic computed tomography, IEEE Trans. Med. Imaging 43 (2) (2024) 771–783.
[38] L.V. Wang, H.I. Wu, Biomedical Optics: Principles and Imaging, 2007.
[39] W. Choi, D. Oh, C. Kim, Practical photoacoustic tomography: realistic limitations and technical solutions, J. Appl. Phys. 127 (23) (2020).
[40] G. Wissmeyer, M.A. Pleitez, A. Rosenthal, V. Ntziachristos, Looking at sound: optoacoustics with all-optical ultrasound detection, Light-Sci. Appl. 7 (2018).
[41] P.H. Reza, K. Bell, W. Shi, J. Shapiro, R.J. Zemp, Deep non-contact photoacoustic initial pressure imaging, Optica 5 (7) (2018) 814–820.
[42] Z. Hosseinaee, J.A.T. Simmons, P.H. Reza, Dual-modal photoacoustic imaging and optical coherence tomography [Review], Front. Phys. 8 (2021).

[43] G. Soria, R. Tudela, A. Márquez-Martín, L. Camón, D. Batalle, E. Muñoz-Moreno, E. Eixarch, J. Puig, S. Pedraza, E. Vila, A. Prats-Galino, A.M. Planas, The ins and outs of the BCCAo model for chronic hypoperfusion: a multimodal and longitudinal MRI approach, Plos One 8 (9) (2013) e74631.
[44] Z. Ma, N. Ding, Y. Yu, Y. Ma, X. Yuan, Y. Wang, Y. Zhao, J. Luan, J. Liu, Quantification of cerebral vascular perfusion density via optical coherence tomography based on locally adaptive regional growth, Appl. Opt. 57 (35) (2018) 10117–10124.
[45] S. Kim, C. Lee, S. Han, H.W. Kang, J. Oh, J. Kim, C. Kim, Simultaneous Imaging Using Combined Optical Coherence Tomography (OCT) and Photoacoustic Microscopy (PAM), 2013.
[46] Z. Ma, Z. Meng, Y. Tian, J. Liu, A. Li, Y. Lin, Y. Yu, J. Luan, H. Wang, Y. Zhao, Y. Wang, Evaluation of mannitol intervention effects on ischemic cerebral edema in mice using swept source optical coherence tomography, Photonics-Basel 9 (2) (2022) 81.
[47] E.Z. Zhang, B. Povazay, J. Laufer, A. Alex, B. Hofer, B. Pedley, C. Glittenberg, B. Treeby, B. Cox, P. Beard, W. Drexler, Multimodal photoacoustic and optical coherence tomography scanner using an all optical detection scheme for 3D morphological skin imaging, Biomed. Opt. Express 2 (8) (2011) 2202–2215.
[48] P.J. Marchand, A. Bouwens, D. Szlag, D. Nguyen, A. Descloux, M. Sison, S. Coquoz, J. Extermann, T. Lasser, Visible spectrum extended-focus optical coherence microscopy for label-free sub-cellular tomography, Biomed. Opt. Express 8 (7) (2017) 3343–3359.
[49] S. Hu, K. Maslov, V. Tsytsarev, L.V. Wang, Functional transcranial brain imaging by optical-resolution photoacoustic microscopy, J. Biomed. Opt. 14 (4) (2009).
[50] X. Zhu, Z. Huang, Z. Li, W. Li, X. Liu, Z. Chen, J. Tian, C. Li, Resolution-matched reflection mode photoacoustic microscopy and optical coherence tomography dual modality system, Photoacoustics 19 (2020) 100188.
[51] J.C. Zhou, J.V. Jokerst, Photoacoustic imaging with fiber optic technology: a review, Photoacoustics 20 (2020).

Ning Ding is a Ph.D. student at Northeastern University, College of Information Science and Engineering. She received her bachelor's degree in Biomedical Engineering from Northeastern University in 2017. Also, she received her master's degree in Biomedical Engineering from Northeastern University in 2020. Her research interest focuses on optical coherence tomography and photoacoustic imaging.

Huiwen Jiang received her bachelor's degree in Biomedical Engineering from Northeastern University, China, in 2018. She is now a Ph.D. candidate in Control Science and Engineering at the School of Information Science and Engineering, Northeastern University. Her research interest is optical coherence tomography.

Ben Xiang received a Bachelor's degree in Automation from Yanshan University in 2020 and he is now a Ph.D. student at Northeastern University, College of Information Science and Engineering. His interest focuses on optical coherence tomography system and OCT angiography.

Yao Yu is a lecturer at School of Control Engineering, Northeastern University at Qinhuangdao, China. She was a Postdoctoral Associate in Thrombosis and Haemostasis lab group in Imperial College London (2013–2014), and received her doctorate degree in Clinical Medicine Research (Investigative Science) in 2013 from Imperial College London. Her main research interests are Alzheimer's disease, diabetic retinopathy, thrombosis, vascular diseases and optical coherence tomography.

Cheng Ji is a chief physician in Qinhuangdao HaiGang hospital. She received her Master degree from Tianjin Medical University. She has been worked in Cardiology Department, and currently is the leader of the Hypertension Department. Her main research interests are Hypertension and cardiovascular and cerebrovascular diseases.

Jian Liu is an associate professor of Control Science and Engineering at Northeastern University at Qinhuangdao. He received his PhD degree from Shenyang University of Technology in 2014. His current research interests include optical coherence tomography.

Yuqian Zhao received the Ph.D. degree in mechanical design theory from Yanshan University, Qinhuangdao, China in 2012. She was an associate professor in school of control engineering, Northeastern University. Her research interest includes analysis of vascular stress state based on multi field coupled simulation model advanced manufacturing processes and their reliability.

Jingmin Luan received the Ph.D. degree in Electronic Information Engineering from Yanshan University, Qinhuangdao, China. His current research interests include Biomedical Signal Processing, Deep Learning.

Yanqiu Yang received the Ph.D. degree in biomedical engineering from Northeastern University, Shenyang, China in 2023. She is currently a lecturer with Northeastern University. Her research interests include the exploration of medicinal substances of national medicines and traditional Chinese medicines, the pharmacological effects of bioactive substances on central neurodegenerative disease, and refining drug and disease markers through the integration of bioinformatics and molecular docking techniques.

Yi Wang is a professor of biomedical engineering at Northeastern University at Qinhuangdao. He received his PhD degree from Xi'an Jiaotong University in 2002. His current research interests include photoacoustic imaging and optical coherence tomography.

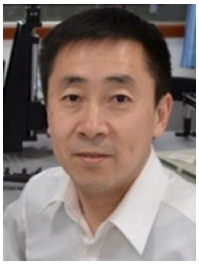

Zhenhe Ma is a Professor and Ph.D. supervisor at School of Control Engineering, Northeastern University at Qinhuangdao. He received the Ph.D. degree in physical electronics from Tianjin University, in 2007. He was a Postdoctoral fellow at the Oregon Health & Science University (2009–2010). His main research directions are optical coherence tomography, photoacoustic imaging, optical imaging and measurement and signal processing.